JOURNAL OF MATERIALS SCIENCE **37** (2002) 1649–1660

Simulation of porosity by microballoon dispersion in epoxy and urethane: mechanical measurements and models

M. A. EL-HADEK, H. V. TIPPUR*
Department of Mechanical Engineering, 202 Ross Hall, Auburn University, AL 36849, USA
E-mail: htippur@eng.auburn.edu

Effective mechanical properties of microballoon-dispersed epoxy and urethane are studied under quasi-static and dynamic loading conditions. Elastic modulus measurements of these mixtures over a volume fraction range of 0–0.45 are in good agreement with Hashin-Shtrikman lower-bound predictions for two-phase mixtures comprising of randomly distributed spherical pores in an elastic matrix. The measurements have also been predicted accurately by a LEFM based pore-flaw model for a selected flaw size to pore size ratio. These imply that the microballoons offer negligible reinforcement due to extremely small wall thickness to diameter ratio. Accordingly, feasibility of using these materials to simulate controlled porosity for tensile strength and fracture toughness modeling is explored. Measured tensile strength and fracture toughness values decrease monotonically similar to the Young's modulus variation with volume fraction of microballoons. Guided by the measurements linear elastic models for porous materials that predict tensile strength and fracture toughness of these mixtures are proposed and validated. The tensile strength predictions are in very good agreement with measurements for both epoxy and urethane compositions. The quasi-static crack initiation toughness prediction captures the measurement trends rather well in both cases. The agreement between the measurements and predictions are modest for epoxy matrix while they are good for urethane compositions. Based on fracture surface micrography, an empirical corrective procedure is advanced to improve the agreement between the measurements and the model. The dynamic crack initiation toughness measurements for epoxy, on the other hand, are in excellent agreement with the predictions.

1. Introduction

Porosity in dense engineering materials is often undesirable for load-bearing applications. In other instances porosity is highly beneficial for weight and cost reduction, enhancing damping and thermal characteristics and, improving specific strength. Examples of natural processes taking advantage of distributed porosity, as in human bone [1] and wood, are also abundant. Inspired by these biological materials, attempts to create porous metallic implants of high degree of compatibility with human tissue are also reported [2, 3]. However, research in this area continues as the mechanical properties of these deteriorate to a greater proportion with the introduction of porosity [4, 5].

Designing for optimum specific stiffness and/or specific strength is an important goal in engineering [6] where modeling mechanical properties of porous materials assumes great deal of significance. Influence of porosity on brittle systems such as ceramic matrix composites is well documented in a recent monograph by Rice [7]. Among the early investigations into the mechanical characterization of cellular materials, Gibson *et al.* [8] have presented mechanics based analyses of two-dimensional honeycomb structures. They have considered bending, buckling and plastic collapse of cell walls ('struts') for developing expressions for effective mechanical properties. It is shown that ratio of the properties of the cellular material relative to that of the 'strut' are of the form $C(\rho/\rho_s)^q$, where ρ is the effective density, ρ_s is the density of the wall material, C and q are constants dependent on cell geometry. Using dimensional arguments, Gibson and Ashby [9] have subsequently extended this concept to three-dimensional cellular materials where the constant C is determined experimentally. In their later work, Maiti *et al.* [10], have introduced a semi-empirical relationship that also shows that fracture toughness ratio of the cellular material relative to its wall properties to depend on the density ratio. Krstic and Erickson [11, 12] have taken a linear elastic fracture mechanics approach for predicting Young's moduli in elastic porous solids wherein cylindrical and spherical pores are assumed to possess radial

*Author to whom all correspondence should be addressed.

and annular flaws, respectively. Using elasticity solutions for cavities in finite size bodies and crack opening displacement concept, models have been developed and verified with experimental data. Effective elastic moduli of metal-matrix composites with damaged particles are estimated by Tong and Ravichandran [13] using modified micro-mechanics procedures in uniaxial and hydrostatic tensile fields which can also be applied to situations with voids as well as damaged particles. Nielsen [14] has established relationships between Young's modulus and strength of porous materials for aiding non-destructive evaluation of porous materials. In all these works, material properties have been shown to monotonically decrease with volume fraction of the pores in the matrix.

Development of materials having controlled porosity (pore shape, size and volume fraction) for modeling and simulation (with the exception of honeycomb and foam materials) purposes is quite challenging. Polymer burnout method has been utilized by Zimmerman *et al.* [15] to produce spherical pores of mean diameter 100 μm in alumina. Using these samples they have studied crack instability ensuing from pore stress concentration near a free edge. Mechanical response of aluminum MMC with microballoon of 1–2 mm diameter and wall thickness to diameter ratios of the order of 0.1 are studied under uniaxial compression by Kiser *et al.* [16]. High degree compressive energy absorption during failure has been observed. Parameswaran and Shukla [17] have used relatively thick-walled cenospheres (mean diameter 127 μm and wall thickness 10–15 μm) in a polyester matrix to create functionally graded material. They have measured effective Young's moduli, failure strengths and fracture toughness for different filler volume fractions. Although particulate composite density decreases with volume fraction, increasing tensile modulus and fracture toughness suggest reinforcement of the matrix by the filler particles in case of Ref. [17].

In the current work, mechanical properties of microballoon-dispersed epoxy and urethane are measured. Apparent tensile modulus, tensile strength and fracture toughness are measured for different volume fractions in the range 0 to 0.45. Based on the measurements feasibility of simulating controlled porosity in these polymers is examined by evaluating the measurements relative to micromechanics models reported in the literature. Subsequently, simple analytical models are proposed for predicting tensile strength and fracture toughness of porous brittle materials and validated by the measurements.

2. Material preparation

Two types of polymeric sheets infiltrated uniformly but randomly with microballoons were prepared. The volume fraction, $V_f (= V_{\text{microballoons}}/(V_{\text{matrix}} + V_{\text{microballoons}}))$, of the microballoons in these sheets ranged between 0 and 0.45. The microballoons used in this investigation were commercially available hollow soda-lime glass spheres of mean diameter $\sim$60 μm and wall thickness of the order of 100 nm ($\sim$400 nm). A typical micrograph of these fillers is shown in Fig. 1. As it will be demonstrated in the subsequent sections, extremely small wall thickness relative to the diameter these fragile fillers make it suitable for modeling the mixture as a porous material with a relatively high degree of accuracy under tensile loading conditions. Other physical and mechanical properties of the constituents are listed in Table I.

Two different thermoset polymers namely, two-part epoxy and urethane were used as matrix materials in this investigation. Each of these resins have relatively

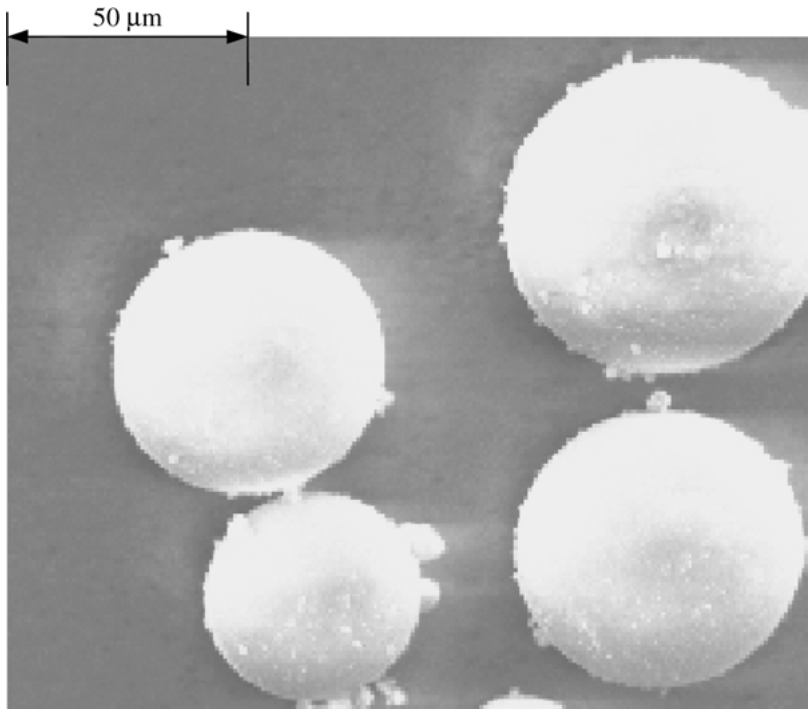

Figure 1 SEM micrographs of microballoons.

TABLE I Properties of the constituents

Properties	Microballoons[a]	Epoxy	Urethane
Mean size	~60 μm	–	–
Wall thickness	~400 nm	–	–
K_{Ic} (MPa$\sqrt{m}$)	0.7	1.1 ± 0.1[b]	–
Tensile modulus (MPa)	–	3016[b]	–
Tensile strength (MPa)	–	58[c]	37[d]
Density (g/cc)	0.13	1.18	1.08[d]
Viscosity (centipoises)	–	213[c]	546.7[d]

[a]3M Corp., Minneapolis, MN.
[b]Reported by R. Young and P. Beaumont [17].
[c]Buhler Inc., USA.
[d]CONAP Inc., USA.

low viscosity at room temperature and long duration (72 hours for epoxy and 168 hours for urethane) curing profiles thereby minimizing residual stresses in the cured material. Manufacturer recommended ratios of resin and hardener were used for material preparation. Sufficient care was exercised to prevent trapping air pockets in the mixture. Once the mixture gelled partially, it was poured into 100 mm × 76 mm × 6 mm size mold and allowed to completely cure. Measurement of longitudinal wave speeds ($\propto \Phi[\sqrt{(E/\rho)}, \nu)]$, E, ν and ρ being Young's modulus, Poisson's ratio and density, respectively) using ultrasonic pulse echo technique at discrete locations of each cured sheet was used as a means of ensuring homogeneity of the material. Sheets with wave speed variation of $\pm 2.5\%$ over the length of the sheet were considered homogeneous and utilized for further investigation.

3. Material characterization

3.1. Tensile tests

The stress-strain responses of materials with different volume fractions were measured from uniaxial tensile tests (Fig. 2) performed accordingly to ASTM standard D-638 for rigid plastics. Standard dog-bone samples were machined according to the dimensions shown in Fig. 3. The tests were carried out at room temperature using Instron Testing Machine (Model 4465) fitted with a 5 kN load cell operating in the displacement control mode. The cross-head speed was 0.25 mm/min. The tests were repeated with three samples for each volume fraction. The stress-strain responses for un-filled epoxy and urethane are shown in Fig. 4. Urethane is significantly compliant compared to epoxy and has a relatively nonlinear elastic response. For selected mix-

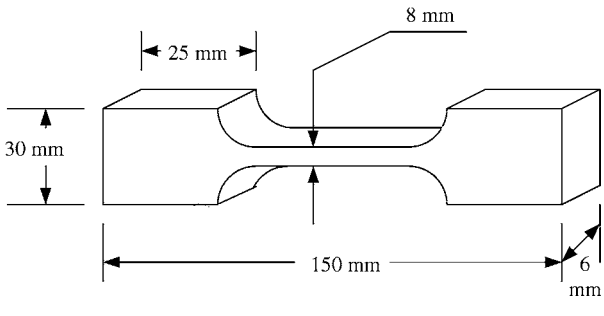

Figure 2 Tension test specimens.

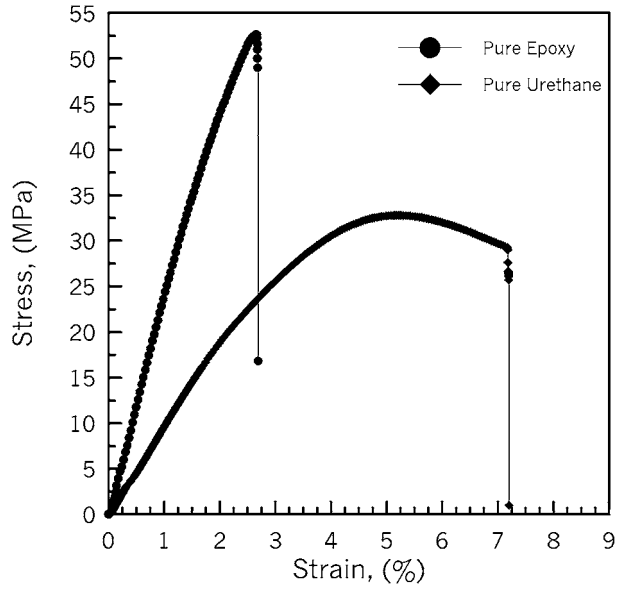

Figure 3 Uniaxial stress-strain response for unfilled epoxy, urethane.

tures of epoxy and urethane with microballoon volume fraction, stress-strain responses are shown in Fig. 4a and b. The plots are essentially linear for epoxy mixtures while modest nonlinearity prior to failure is evident in urethane compositions.

As the volume fraction of the microballoons in the matrix increase, the failure stresses and strains decrease. Further, this leads to the reduction of the Young's modulus and an increase of the elastic strain at a given stress. This has been explained by Krstic and Erickson [12] as a consequence of crack opening displacement caused by the presence of radial and/or annular cracks associated with pores. The failure strains are noticeably higher in urethane mixtures compared to epoxy samples. The opposite is true when the tensile strengths of these two materials are considered.

3.2. Elastic modulus—quasi-static measurements

Young's moduli were determined from uniaxial stress-strain responses and are plotted as solid symbols in Fig. 5a and b for epoxy and urethane samples. The values of the Young's moduli for unfilled polymers in both cases agree well with the values reported in the literature [18]. The values decrease monotonically with microballoon volume fraction over the entire range. Approximately 60% reduction in the Young's modulus between infiltrated ($V_f \sim 0.45$) and unfilled polymers are evident.

To investigate the feasibility of using microballoon dispersion as a means of introducing controlled porosity in these polymers, comparison of the measurements with micro-mechanics predictions based Hashin-Shtrikman lower bound estimation [19–21] was carried out. It should be noted that, for spherical filler particles in two-phase compositions, lower bounds are known to offer accurate prediction of apparent Young's modulus [20] and hence recommended. For a two-phase mixture comprising of matrix and spherical fillers, the apparent bulk (B) and shear (μ) moduli are expressed in terms

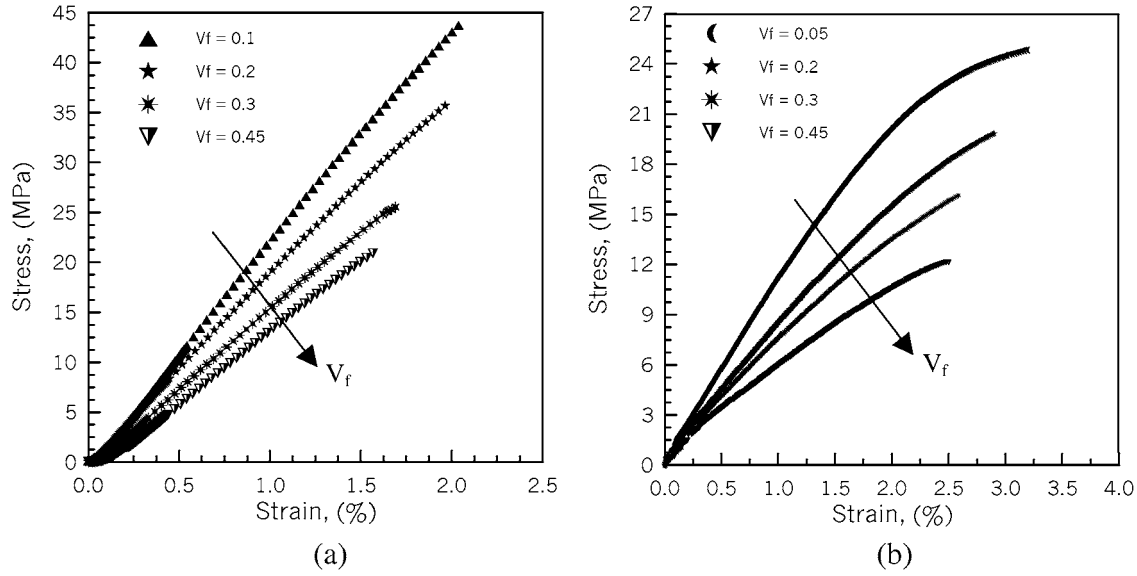

Figure 4 Stress-strain curves for microballoon-dispersed (a) epoxy compositions, (b) urethane compositions.

of the corresponding properties of the matrix (subscript 'm') and filler (subscript 'f') as,

$$B_c = B_f + \frac{V_f}{\dfrac{1}{B_m - B_f} + \dfrac{3(1 - V_f)}{3B_m + 4B_f}}, \tag{1}$$

$$\mu_c = \mu_f + \frac{V_f}{\dfrac{1}{\mu_m - \mu_f} + \dfrac{3(1 - V_f)(B_m - 2\,\mu_m)}{5\,\mu_m(3B_m + 4\,\mu_m)}}, \tag{2}$$

where V_f is the filler volume fraction and subscript 'c' denotes the properties of the mixture. Now, bulk and shear modulus estimates of the porous material in terms of pore volume fraction and properties of the matrix were determined by setting values of B_f and μ_f equal zero in Equations 1 and 2. Subsequently, the Young's modulus was determined from the apparent bulk and shear moduli using,

$$E_c = \frac{9B_c\mu_c}{3B_c + \mu_c}. \tag{3}$$

The comparison between micro-mechanics predictions (solid line) and experimental measurements (solid symbols) are shown in Fig. 5. Excellent agreement between the two sets of data is evident over the entire range of volume fractions studied. The maximum difference between the predictions and measurements in each case is less than 10%. The agreement also suggests negligible reinforcement of both epoxy and urethane compositions by the microballoons and hence allows further investigation of these compositions as porous materials.

Also shown in Fig. 5 are the Young's modulus predictions by Gibson and Ashby [8] for cellular solids and modified Mori-Tanaka approach [22] for two-phase

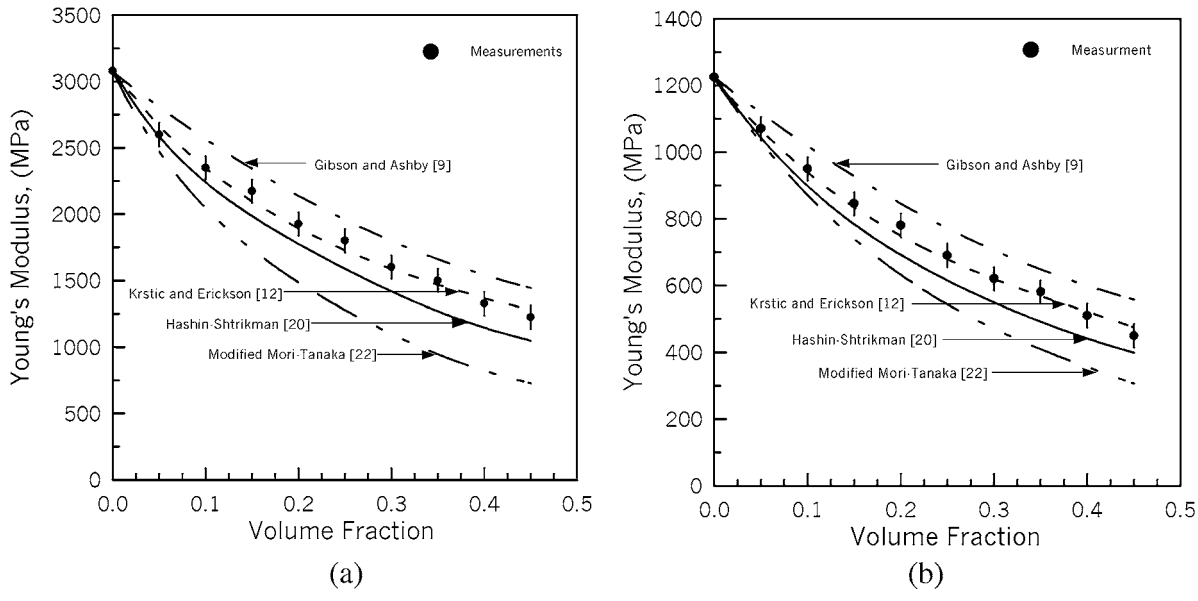

Figure 5 Comparison between predicted and measured quasi-static Young's moduli for microballoon-dispersed (a) epoxy, (b) urethane compositions.

mixtures with filler phase properties set equal to zero. Substantial under prediction of Young's moduli by the latter is evident for both epoxy and urethane mixtures. On the contrary the cellular material model [8] over predicts the measurements consistently but fairly accurately. As discussed in the Introduction, a pore-flaw model that accounts for stress concentration effects near a pore along with crack opening displacements has been proposed by Krstic and coworkers [12, 23, 24] to explain the Young's modulus reduction. In these, the Young's modulus of the porous material is given by,

$$E_c = E_m\left[1 + \frac{16N_pR^3\left(1-\nu_m^2\right)}{3}\phi\right]^{-1}, \qquad (4)$$

where ϕ is a function that depends on the flaw size s and the pore radius R as follows:

$$\phi = \left(1+\frac{s}{R}\right)^3 + \frac{9}{2(7-5\nu)\left(1+\frac{s}{R}\right)^2} + \frac{4-5\nu}{2(7-5\nu)},$$

and

$$N_p = \frac{3V_f}{4\pi R^3}. \qquad (5)$$

In Equations 4 and 5, the flaw of size s is assumed to be a hemispherical annular crack subjected to the stress field in the vicinity of a spherical pore in an elastic body. The Young's modulus values calculated using this model were found to agree well with the measured ones when $s/R \sim 0.26$ and $s/R \sim 0.22$ for epoxy and urethane compositions, respectively. The comparison is shown as broken line in Fig. 5. It should be pointed out, however, that in the absence of systematic guidelines on the choice of s/R values and the experimental difficulty in determining such as value, the values selected were based on trial and error.

3.3. Elastic modulus—dynamic measurements

The values of apparent dynamic Young's moduli (E^d) for epoxy and urethane compositions were also determined for completeness. These values were determined by measuring longitudinal (C_l) and shear (C_s) wave speeds,

$$C_l^2 = \frac{E^d}{\rho}\frac{(1-\nu)}{(1+\nu)(1-2\nu)}, \quad C_s^2 = \frac{E^d}{\rho}\frac{1}{2(1+\nu)}, \qquad (6)$$

in these materials using ultrasonic pulse-echo technique. In the above, ρ and ν denote apparent density and Poisson's ratio, respectively. The ultrasonic transducers of crystal diameter 3 mm and 5 mm, operating at frequencies of 10 MHz and 2.25 MHz, respectively, were used for epoxy and urethane. The measurements were used in conjunction with measured densities of different mixtures and equations (6) to determine dynamic Young's modulus and Poisson's ratio. Incidentally, the variation in the value of Poisson's ratio was found to be small in the range 0.35 ± 0.01.

The variation of apparent dynamic Young's moduli with volume fraction is shown in Fig. 6 and is similar to the ones seen for quasi-static counterparts. Due to the rate dependency of the matrix materials, the values of Young's modulus are consistently higher for both types of mixtures when compared to their quasi-static counterparts shown in Fig. 5. The reduction in the values of E^d between unfilled and the mixture with $V_f = 0.45$ for both epoxy and urethane is again ~60%. Shown in Fig. 6, are the Hashin-Shtrikman predictions [20] for two-phase mixtures with the elastic properties of the filler set equal to zero, thereby representing predictions for porous materials. Excellent agreement between the

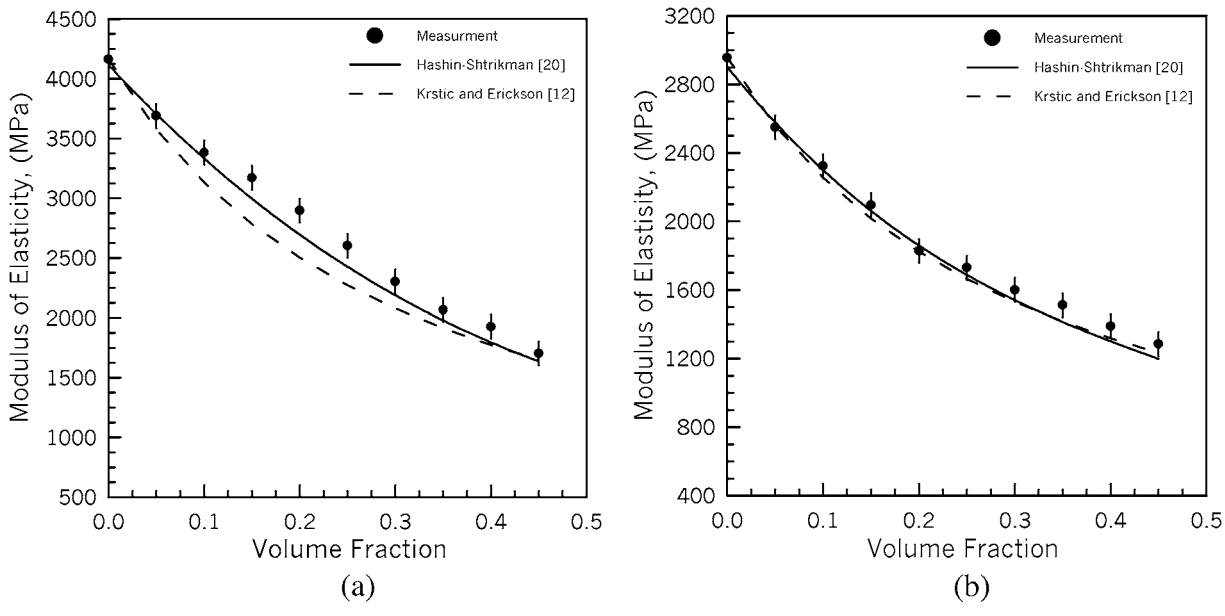

Figure 6 Comparison between predicted and measured dynamic Young's moduli for microballoon-dispersed (a) epoxy, (b) urethane compositions.

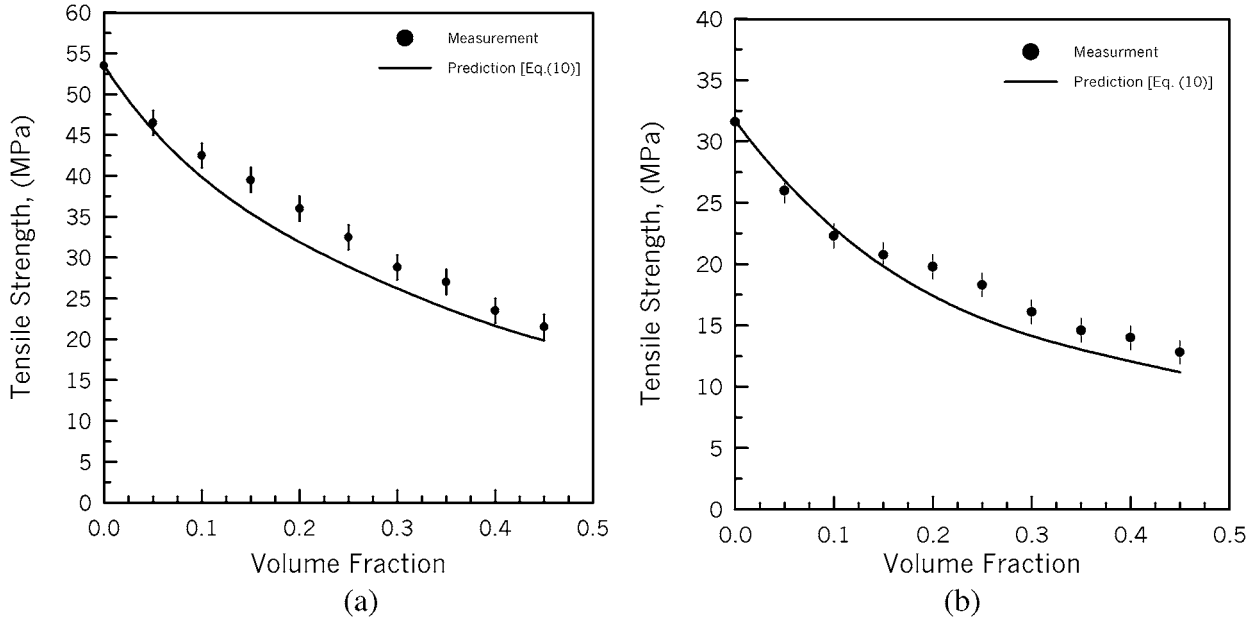

Figure 7 The variation of tensile strength of microballoon-dispersed (a) epoxy, (b) urethane compositions with volume fraction.

measurements and predictions are seen and reinforcement of the matrix by the filler, if any, is therefore negligible. Also, shown in Fig. 6 are the predictions based on the pore-flaw model (Equation 4) for the same s/R values used in quasi-static counterparts. Evidently, the agreement between the two is good.

4. Tensile strength

From the stress-strain responses shown in Fig. 4, apparent tensile strengths, $(\sigma_c)_{\rm cr}$, of epoxy and urethane compositions were also measured. The variation of tensile strengths with volume fraction of microballoons is shown in Fig. 7 by solid symbols. Nonlinear monotonic reduction in the apparent tensile strength with filler volume fraction over the entire range is observed. Maximum strength reduction of approximately 60% in both epoxy and urethane relative to unfilled matrix are evident. Notably, the trends are similar to the variation of Young's modulus shown in Fig. 5. This phenomenological observation forms the basis for a simplified predictive model for tensile strength described next.

Predictive models for the apparent tensile strength of particle reinforced composites are very limited (Nielsen [14], Gibson and Ashby [9]). In the present work, a strain energy based model is proposed for predicting the strength of brittle porous bodies. Consider a porous linear elastic sheet, shown schematically in Fig. 8. Let the material have a random distribution of spherical cavities throughout the matrix. Now, consider a tensile stress $\sigma_{\rm c}$ acting on this sheet normal to the nominal cross-section area $A(=b \times t$, width and thickness, respectively). The corresponding apparent tensile strain be $\varepsilon_{\rm c}$. Within the control volume $(L \times b \times t)$, the average reduced cross-section area normal to the far-field stress be $\langle A' \rangle (=\langle b' \rangle \times \langle t' \rangle)$ due to the presence of cavities in the material with $\langle \bullet \rangle$ denoting ensembled average. Then, recognizing that the overall strain energy stored in the porous composition is equal to that in the matrix material, for linear elastic material behavior and plane strain conditions,

$$AL\left(\frac{1}{2}\sigma_c\varepsilon_c\right) = \langle A' \rangle L\left\langle\frac{1}{2}\sigma_x\varepsilon_x + \frac{1}{2}\sigma_y\varepsilon_y + \frac{1}{2}\sigma_{xy}\gamma_{xy}\right\rangle_m \tag{7}$$

where x, y denote in-plane Cartesian coordinates of the porous sheet as shown. By recognizing that strain energy in the matrix can be approximated by the dominant first term to a high degree of accuracy (see, Appendix), the right hand side of Equation 7 can be simplified as,

$$AL\left(\frac{1}{2}\sigma_c\varepsilon_c\right) \approx \langle A' \rangle L\left\langle\frac{1}{2}\sigma_x\varepsilon_x\right\rangle_m \equiv \langle A' \rangle L\left(\frac{1}{2}\langle\sigma_m\rangle\langle\varepsilon_m\rangle\right). \tag{8}$$

In the above, for simplicity the subscript 'x' has been dropped and $\langle\sigma_m\rangle$ and $\langle\varepsilon_m\rangle$ denote the average values of matrix stress and matrix strain components, respectively. The above simplification implicitly takes into account the reduction in stress concentration effects with decreasing separation distance between pores [25]. Now, recognizing that $\sigma_c A = \langle\sigma_m\rangle\langle A' \rangle$, Equation 7 becomes,

$$\varepsilon_c \approx \langle\varepsilon_m\rangle. \tag{9}$$

Equation 9 implies that the apparent strain in the porous medium is approximately equal to the average matrix strain component in the x-direction. Accordingly, Equation 7 can be expressed as,

$$\sigma_c = \frac{E_c}{E_m}\langle\sigma_m\rangle \Rightarrow (\sigma_c)_{\rm cr} = \frac{E_c}{E_m}(\langle\sigma_m\rangle)_{\rm cr}, \tag{10}$$

where $(\sigma_c)_{\rm cr}$ denotes the apparent tensile strength of the mixture and $(\langle\sigma_m\rangle)_{\rm cr}$ is the tensile strength of the matrix. Thus, the tensile strength of the porous composition is

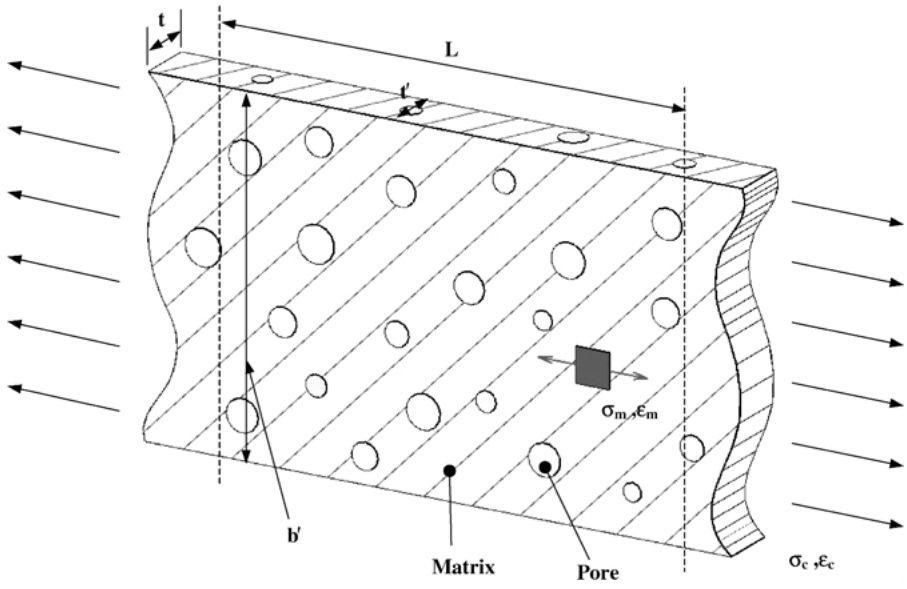

Figure 8 Uniaxial tension model to predict tensile strength.

described in terms of the Young's modulus ratio of the porous and matrix materials and, tensile strength of the matrix. It should be noted that in Equation 10, the matrix strength of the matrix material being constant, the strength of the mixture is dependent on the volume fraction of the cavities in the mixture through Young's modulus of the mixture ($E_c \equiv E_c(V_f)$). This is similar to the observations made by Nielsen [14] that Young's modulus and strength of porous materials are directly related.

4.1. Experimental validation

The validity of the proposed model is demonstrated in Fig. 7 for both the polymers. Evidently, good agreement of generally better than 10% deviation between the measurements and Equation 10 (solid line) is seen for the entire range of volume fractions studied. Accordingly, one could conclude, that despite its simplicity, the proposed model is indeed able to capture the essential features of tensile strength behavior effectively for these two material systems modeled as porous solids.

Krstic [24] has also proposed an expression for predicting the tensile strength of porous materials with spherical cavities of diameter D as,

$$(\sigma_c)_{\mathrm{cr}} = \frac{1}{\phi}\left[\frac{\pi E_c \gamma}{D\left(1+\frac{s}{R}\right)\left(1-\nu_c^2\right)}\right]^{1/2} \qquad (11)$$

where ϕ is geometric function given by Equation 5, and γ is the fracture energy of the matrix. Again, linear elastic fracture mechanics approach was used in deriving Equation 11 where the existence of annular flaw (of size s) around the spherical pore was assumed. The predicted values of the tensile strength using $s/R \sim 0.26$ and $s/R \sim 0.22$ for epoxy and urethane compositions, respectively, however, deviate substantially from the measurements and therefore not shown. Further, predictions based on Equation 11 for the s/R values mentioned in the previous section over estimate the strength. In order for the model to agree with the measurements, one has to select a significantly different value of $s/R(\sim 0.7)$ from the one used for predicting Young's modulus in Figs 5 and 6. One could, however, see the applicability of pore-flaw model (Equation 4) for predicting strength in from a different perspective. Since the predicted values of E_c of the porous material based on Equation 4 agree well with the measurements, one could utilize Young's modulus predictions in Equation 10 for successfully predicting the measured strength (and Equation 15 for predicting critical stress intensity factors, to be discussed in the next section). This in turn would incorporate the pore-flaw concept in the strength prediction process.

5. Critical stress intensity factors

Another important aspect of the mechanical behavior of porous materials is the fracture response. The crack initiation toughness or critical stress intensity factors $(K_{\mathrm{I}})_{\mathrm{cr}}$ in microballoon filled epoxy and urethane with respect to the pore volume fraction were determined using three-point bending tests. Edge notched beams, shown schematically in Fig. 9, were prepared for selected volume fractions up to 0.45. In each specimen, an

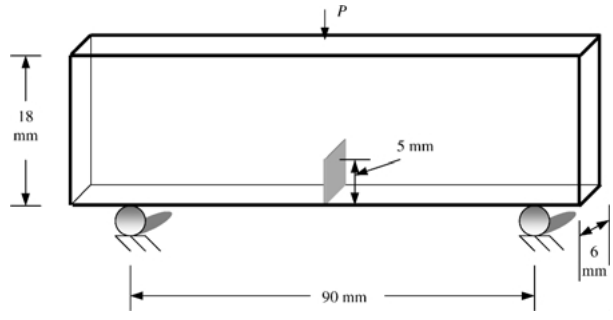

Figure 9 Loading configuration and geometry of single edge notched specimen.

initial notch of root radius 75 μm and length 5 mm was introduced using a high-speed diamond-impregnated circular saw. The notch was subsequently extended into a sharp crack by gently tapping-in a wedge into the mouth of the notch forcing the crack tip to 'pop' by a few millimeters and arrest. Care was exercised to ensure the tip of the wedge from contacting the tip of the notch during crack extension, thereby preventing undue residual deformations at the crack tip. The cracked samples were loaded in an Instron Testing machine with displacement controlled loading and quasi-static loading history was recorded using a PC-based DAQ system. Typically five samples were tested for each volume fraction and the failure load ($P_{\rm cr}$) in each case was used to determine crack initiation toughness using [26],

$$(K_{\rm I})_{\rm cr} = f\left(\frac{a}{W}\right)\frac{P_{\rm cr}S}{BW^{3/2}}, \tag{12}$$

with the geometric factor $f(a/W)$ given by,

$$f\left(\frac{a}{W}\right) = \frac{3\sqrt{\frac{a}{W}}\left(1.99 - \frac{a}{W}\left(1-\frac{a}{W}\right) - 2.15 - 3.93\frac{a}{W} + 2.7\left(\frac{a}{W}\right)^2\right)}{2\left(1+\frac{a}{W}\right)\left(1-\frac{a}{W}\right)^{3/2}}.$$

In the above, a, S, B and W are crack length, span, thickness and height of the beam samples (see Fig. 9), respectively. The apparent critical stress intensity factors, $[(K_{\rm I})_{\rm cr}]_c$, determined from the above are plotted as a function of volume fraction of the microballoons in Fig. 10a and b for epoxy and urethane mixtures, respectively. The measurements monotonically decrease with increasing volume fraction of the microballoons. This trend is similar to the observation of other investigators for brittle ceramics having different degrees of porosity [27, 28]. The values of $[(K_{\rm I})_m]_{\rm cr}$ for unfilled epoxy and urethane are approximately 1.2 MPa$\sqrt{\rm m}$ and 1.45 MPa$\sqrt{\rm m}$, respectively. The measured value for the epoxy is also in good agreement with those reported in the literature for quasi-static loading conditions [18]. For epoxy, the reduction $[(K_{\rm I})_{\rm cr}]_c$ for V_f ranging 0–0.45, is nearly 40% while for urethane it is about 58%. These percentage reductions, particularly in case of epoxy, are somewhat lower than the ones seen for tensile strength over the same V_f range. Crack initiation toughness being a local material characteristic, fracture surface micrographs were studied in order to reconcile this observation and will be discussed later.

As done with tensile strength, a simple model to predict critical stress intensity factors for brittle porous materials based on linear elastic fracture mechanics is proposed. The phenomenological observation that $[(K_{\rm I})_{\rm cr}]_c$ values decrease monotonically with microballoon population similar to Young's modulus and tensile strength values is utilized in proposing this model. The apparent stress intensity factor for a generic mode-I crack in a microballoon-dispersed mixture is,

$$(K_{\rm I})_c = \sigma_c\sqrt{\pi a}, \tag{13}$$

where a is the flaw size. Now, from Equation 10 σ_c can be expressed in terms of σ_m to get,

$$(K_{\rm I})_c = \frac{E_c}{E_m}\langle\sigma_m\rangle\sqrt{\pi a}. \tag{14}$$

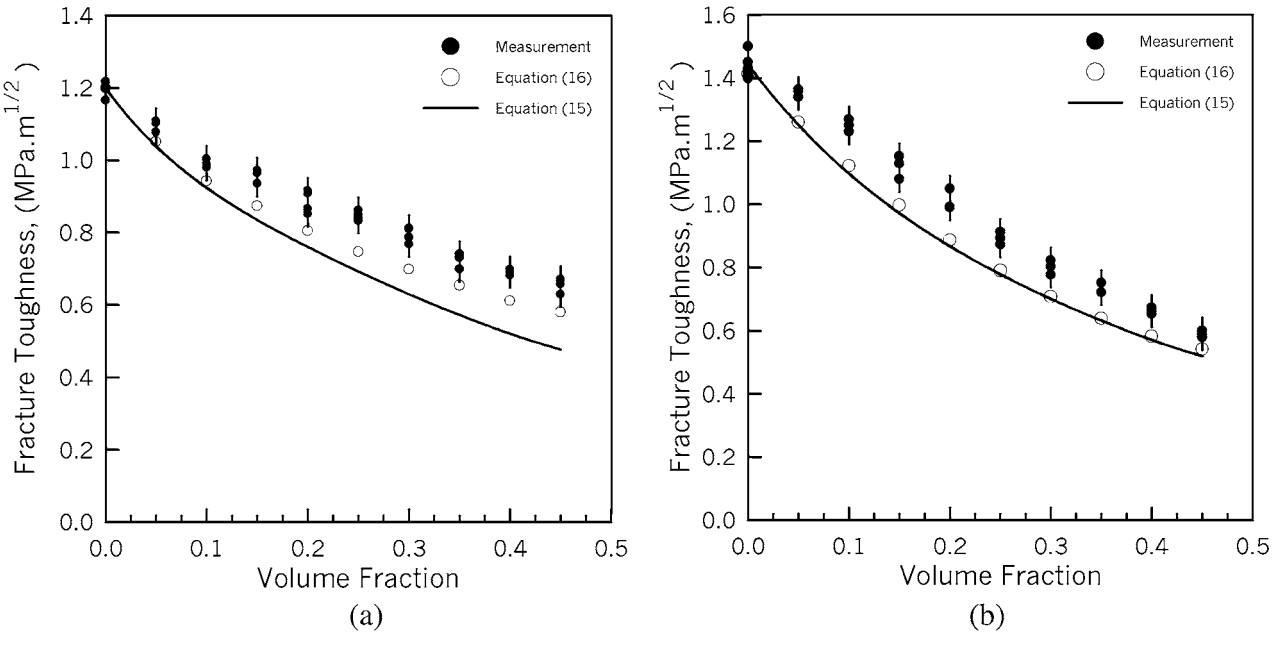

Figure 10 Predicted and measured effective crack initiation toughness of microballoon-dispersed (a) epoxy, (b) urethane.

The critical value of apparent stress intensity factor for the porous composition $[(K_{\mathrm{I}})_{\mathrm{cr}}]_c$ can then be expressed as,

$$\left[(K_{\mathrm{I}})_{\mathrm{cr}}\right]_c = \frac{E_c}{E_m}(\langle\sigma_m\rangle\sqrt{\pi a})_{\mathrm{cr}} = \frac{E_c}{E_m}\left[(K_{\mathrm{I}})_{\mathrm{cr}}\right]_m, \quad (15)$$

where $[(K_{\mathrm{I}})_{\mathrm{cr}}]_m$ is the crack initiation toughness of the matrix material. Thus, Equation 15 suggests that $[(K_{\mathrm{I}})_{\mathrm{cr}}]_c$ variation would be similar to that of the Young's modulus of the porous solid since Young's modulus and crack initiation toughness for the matrix are constant. This is consistent with the earlier observation that experimentally measured values for the mixtures show monotonic reduction in $[(K_{\mathrm{I}})_{\mathrm{cr}}]_c$ similar to the trends for E_c in both epoxy and urethane.

5.1. Experimental validation—quasi-static loading

Solid lines in plots in Fig. 10a and b were obtained from Equation 15 and are superimposed on the experimental measurements. In each case Equation 15 provides a conservative estimate of the apparent crack initiation toughness value for all volume fractions considered. Evidently, the agreement between the measurements and the predictions is only modest for epoxy with better agreement seen at lower volume fractions and increasing deviation with V_f. In case of urethane, on the other hand, the agreement is rather good over the entire range.

As alluded to earlier, fracture behavior being a local crack tip response, micrographs of the fracture surfaces were examined to further ascertain the observations. The fractured surfaces of microballoon-dispersed epoxy and urethane with a volume fraction of 0.25 were studied using SEM. Typical micrographs for the same are shown in Fig 11a and b. The fracture surface morphology reveals that the microballoons have completely fractured in both types of matrix. Further, cleavage fracture in epoxy matrix is readily evident while in case of urethane it is relatively fibrous due to higher degree of material nonlinearity. Interestingly, in case of epoxy mixture, in addition to hemispherical microballoon fracture, *some* also appear to have separated from the surrounding matrix material. This suggests additional dissipation of energy (in addition to matrix and microballoon fracture) during crack initiation and growth. On the contrary, microballoon interfacial separation is minimal in case of urethane mixture. Since all other parameters such as microballoon size, material processing and experimental methods are identical, interfacial energy dissipation is potentially at the root of somewhat larger deviation between experiments and predictions in Fig. 10a. In this context, it should be noted that since nominal fracture toughness value of soda-lime glass ($\sim$0.7 MPa$\sqrt{\mathrm{m}}$ [29]) is significantly lower than that for both the matrix materials and the wall thickness of microballoons being of the order of 100 nanometers, the energy dissipated through microballoon fracture would be a negligible fraction of the total energy for fracture. Accordingly, interfacial separation is a likely source of deviation between measured and predicted values of $[(K_{\mathrm{I}})_{\mathrm{cr}}]_c$. An empirical way of accounting for the deviation is to modify Equation 15 as,

$$\left[(K_{\mathrm{I}})_c\right]_{\mathrm{cr}} - K_{\mathrm{cor}} \equiv \left[(K_{\mathrm{I}})_c\right]'_{\mathrm{cr}} = \frac{E_c}{E_m}\left[(K_{\mathrm{I}})_m\right]_{\mathrm{cr}}, \quad (16)$$

where K_{cor} denotes a stress intensity factor correction that takes into account interfacial separation seen in *some* microballoons. Thus, $[(K_{\mathrm{I}})_c]'_{\mathrm{cr}}$ in Equation16 denote approximate values of apparent stress intensity factors at crack initiation in the absence of any microinterfacial separations. Now, assuming K_{cor} to be of the form, $K_{\mathrm{cor}} \cong \alpha V_f |K_{\mathrm{int}}|$, where α denotes a known fraction of microballoons ($0 \leq \alpha \leq 1$) which show interfacial separation along a typical crack front and $|K_{\mathrm{int}}|$ represents an 'average' value of interfacial crack initiation toughness. Here α can be determined from the micrographs by the percentage of total number of

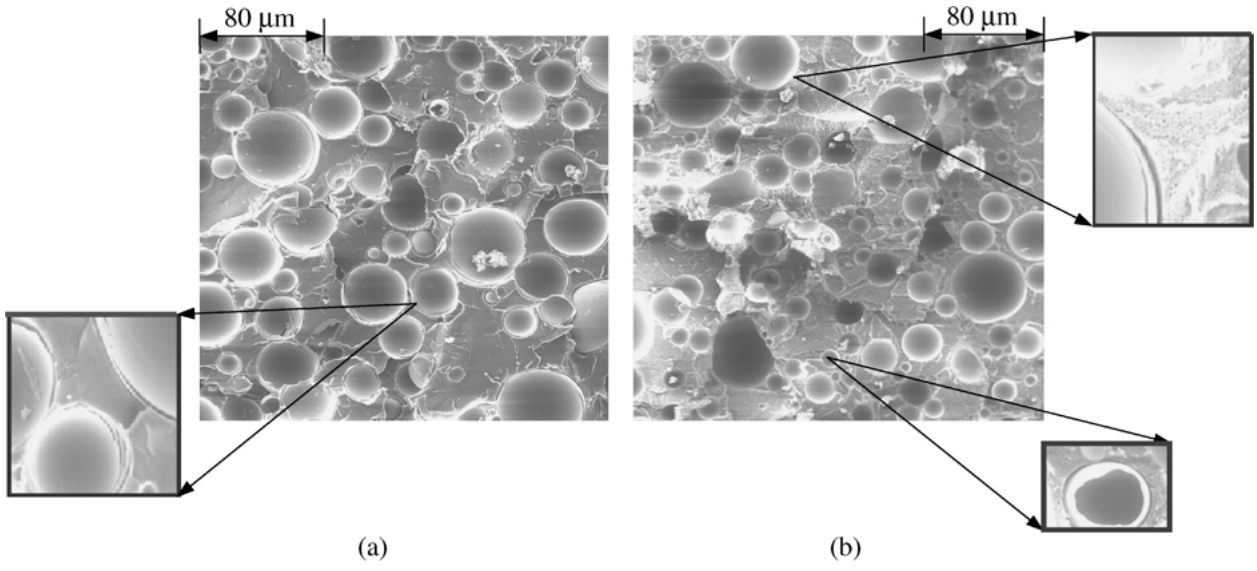

Figure 11 SEM micrographs for (a) epoxy, (b) urethane, infiltrated with microballoons at 0.25 volume fraction (quasi-statically fractured surfaces).

particles showing evidence of separation from the matrix. To proceed further, a value of $|K_{\text{int}}|$ is necessary. It is widely recognized that interfacial fracture process is inherently mixed-mode in nature [30] and interfacial crack initiation toughness generally depends on the local mode-mixity [31]. However, for simplicity, $|K_{\text{int}}|$ was approximated to be constant and equal to the fracture toughness of glass. From the micrographs it was determined that α is $\sim$0.4 in case of epoxy and $\sim$0.2 in case of urethane. Taking these factors into account, values of $K_{\text{cor}}(V_f)$ and corresponding values of $[(K_{\text{I}})_c]'_{\text{cr}}$ were evaluated. The values of the critical stress intensity factor based on Equation 16 are shown in Fig. 10 as open symbols. The agreement between the open symbols and the predictions (solid line) are substantially improved when compared to the solid symbols. A more sophisticated analysis could potentially mitigate the deviation to a greater extent. Alternatively, improving the interfacial strength between the microballoon and the epoxy matrix could eliminate the problem as well.

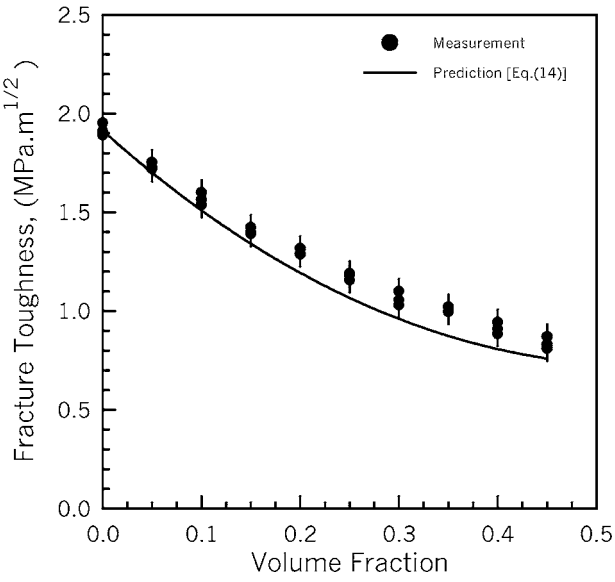

Figure 12 Apparent dynamic crack initiation toughness of microballoon-dispersed epoxy.

5.2. Experimental validation—dynamic loading

Dynamic values of critical stress intensity factors ($[(K_{\text{I}}^d)_c]_{\text{cr}}$) for microballoon-dispersed epoxy were also evaluated. Homogeneous beam (150 mm $\times$ 20 mm $\times$ 6 mm) samples (four specimens for each volume fraction) with single edge notches were prepared. The notches were extended into sharp cracks as described earlier. The samples were subsequently impact loaded (impact velocity of 1.5 m/s) in three-point bending configuration in Instron-Dynatup - 8210 instrumented drop tower. This was achieved by releasing a 90 N (20 lb) deadweight along guide rails from a designated height. Integral to the deadweight is a cylindrical tup, with a hemispherical end of radius 12.7 mm, that impacts the specimen directly on the edge opposite to the crack. Affixed to the tup are sensors that feed information such as time, load and displacement history experienced by the tup to a PC-DAQ system. The maximum load registered at the tup was used to assess the dynamic crack initiation toughness using Equation 12. (The rate of increase in stress intensity factor prior to initiation in all specimens tested was 19 ± 1.8 MPa-$\sqrt{}$m/ms). The measured values of $[(K_{\text{I}}^d)_c]_{\text{cr}}$ for different volume fractions of microballoons are plotted as solid symbols in Fig. 12. Evidently $[(K_{\text{I}}^d)_c]_{\text{cr}}$-$V_f$ variations are qualitatively similar to the ones obtained for quasi-static loading (Fig. 10). That is, values of $[(K_{\text{I}}^d)_c]_{\text{cr}}$ monotonically decrease with V_f and an overall reduction of about

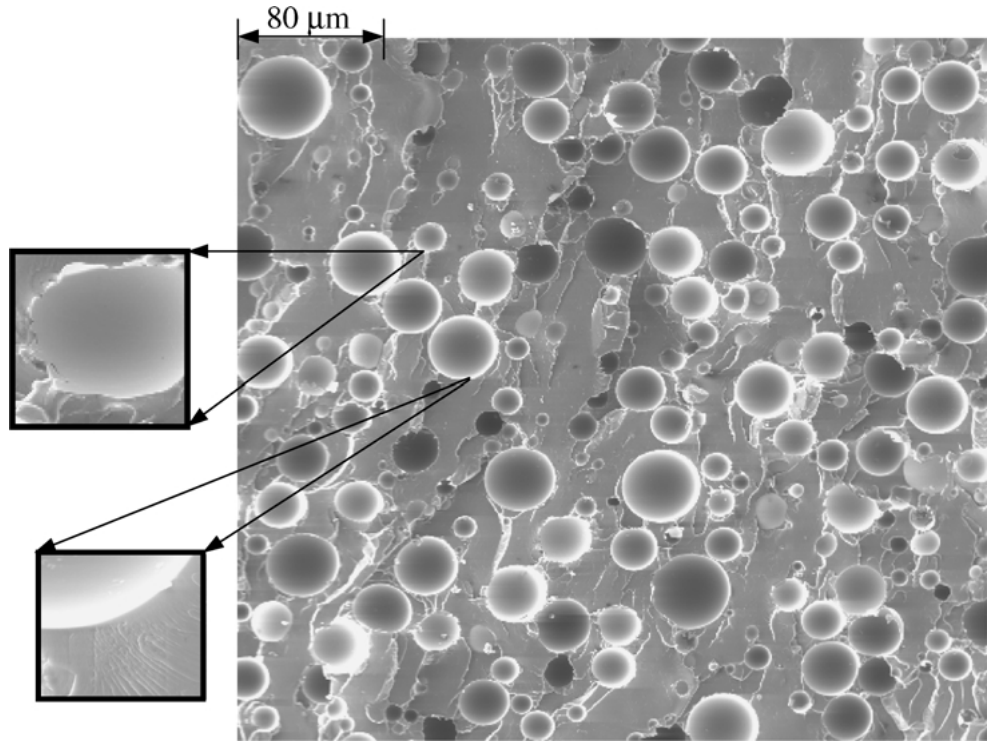

Figure 13 SEM micrographs for epoxy infiltrated with microballoons at 0.25 volume fraction. (dynamically fractured surface).

60% between unfilled and the mixture with $V_f = 0.45$ is seen. The percentage reduction for dynamic fracture tests, however, is comparable to the ones for Young's modulus (Fig. 5a) and tensile strength (Fig. 6a). This, however, is unlike the quasi-static results shown in Fig. 10a. It should be noted that values of $[(K_{\mathrm{I}}^d)_c]_{\mathrm{cr}}$ for each V_f is significantly higher than the corresponding value $[(K_{\mathrm{I}})_c]_{\mathrm{cr}}$ obtained under quasi-static loading conditions, due to the loading rate dependent behavior of epoxy.

Also shown in Fig. 12 are the predicted values (solid line) of $[(K_{\mathrm{I}}^d)_c]_{\mathrm{cr}}$ from Equation 12 for different volume fraction of microballoons. In these calculations, the dynamic Young's modulus values from Fig. 6a were utilized. Evidently, the agreement between the measurements and the predictions is very good over the entire range of volume fractions studied. This is unlike the values for quasi-statically fractured beams (Fig. 10a). To further reconcile this observation, a dynamically fractured sample surface with a microballoon $V_f = 0.25$ was examined microscopically. The corresponding micrograph is shown in Fig. 13. Interestingly, unlike in Fig. 11a, the interfacial separation of the microballoons seen under quasi-static loading conditions is non-existent in the dynamic case and hence the better agreement between the model and the measurements under dynamic conditions. Otherwise, the fracture surface is relatively more rugged when compared to quasi-statically fractured surface accounting for higher expenditure of energy during fracture.

6. Concluding remarks

Possibility of dispersing microballoons in epoxy and urethane to simulate controlled porosity in polymers in a simple and cost-effective way is examined. To this end, homogenous samples with different microballoon volume fractions, ranging from 0 to 0.45, were prepared and tested. Uniaxial tension tests on dog-bone samples and three-point bending on SEN samples were carried out to arrive at the following conclusions:

- The Young's modulus was found to decrease monotonically over the entire range of microballoon volume fractions. The measurements, quasi-static as well as dynamic, are in very good agreement with Hashin-Shtrikman lower-bound predictions for two-phase mixtures comprising of matrix and randomly distributed spherical voids/pores. The pore-flaw model proposed by Krstic and Erickson show good agreement with the measurements as well for flaw size to pore size ratio of 0.26 and 0.22 for epoxy and urethane respectively.
- The tensile strength was found to decreases monotonically with increasing microballoon volume fraction and the trends are akin to the ones observed for Young's modulus. Guided by the experimental observation, a linear elastic model based on strain energy balance has been proposed for predicting tensile strength of brittle porous materials. The model generally predicts the measurements to within 10% for both epoxy and urethane compositions, over the entire range of volume fractions.
- The critical stress intensity factor values measured under *quasi-static loading conditions* were found to continuously decrease with microballoon volume fraction as in case of tensile modulus and strength. Again, based on experimental evidence, a predictive model using linear elastic fracture mechanics has been introduced. A somewhat large deviation between the measurements and predictions in case of epoxy is explained by micrographs that reveal additional expenditure of energy by interfacial separation between microballoons and the matrix. Otherwise, the microballoons generally show hemispherical fracture in both matrix materials. An empirical correction factor based on this observation has been introduced to reduce the difference between the predictions and measurements.
- The critical stress intensity factor values measured *under impact loading conditions* also monotonically decrease with microballoon volume fraction. Unlike quasi-static results, microscopic examination of dynamically fractured surfaces generally showed hemispherical fracture of microballoons and interfacial separation was non-existent. Accordingly, the proposed predictive model for brittle porous materials for critical values of apparent stress intensity factors agrees well with the dynamic measurements.
- The proposed models for tensile strength and fracture toughness of mixtures suggest the variation to be directly proportional to their Young's moduli with volume fraction of the pores. The measurements using in microballoon-dispersed epoxy and urethane support the model.

Appendix

The approximation that under uniaxial remote loading, the energy density $U\ (=\frac{1}{2}(\sigma_x\varepsilon_x + \sigma_y\varepsilon_y + \sigma_{xy}\gamma_{xy}))$ is given by the dominant term $U'(=\frac{1}{2}\sigma_x\varepsilon_x)$ was validated through elasto-static finite element modeling of a porous sheet with an array of distributed *cylindrical*

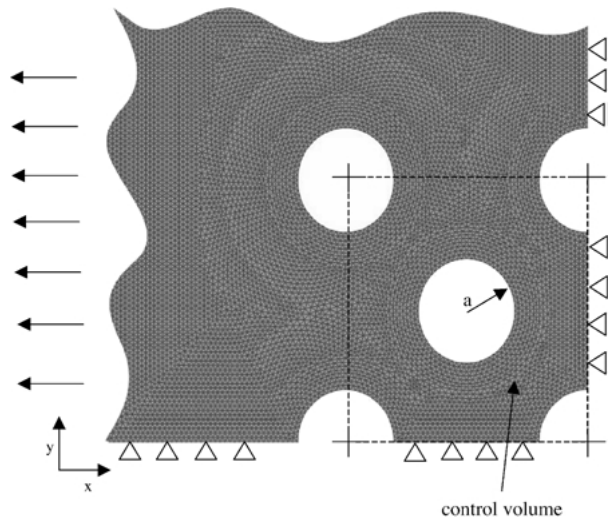

Figure A1 The dimensionless finite element model, where the element size is 40 μm.

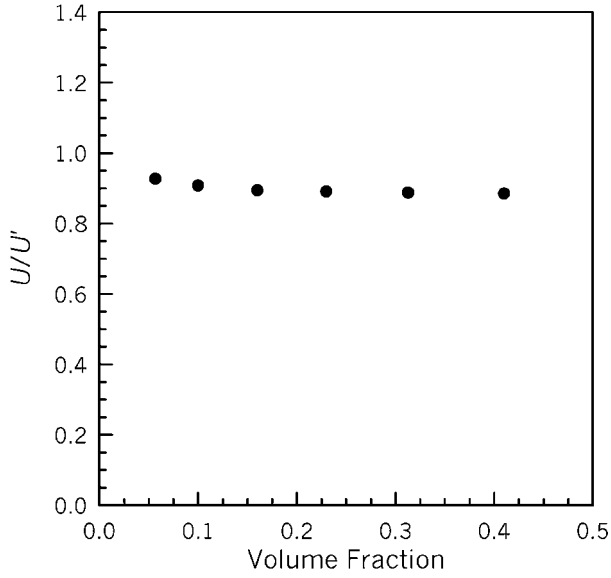

Figure A2 The ratio U'/U with respect to volume fraction.

cavities. The finite element model used for this verification is shown in Fig. A-1. Due to symmetry, a fourth of the model was used in the computations. Two-dimensional plane strain simulations with cylindrical cavities were carried out instead of 3-D simulations involving spherical cavities for (a) simplicity and (b) a more conservative estimate of the error involved in the approximation. (Here it should be noted that analytical solutions for the limiting case of single cavity in an infinite sheet subjected to uniaxial tension indeed suggest a relatively benign stress concentration effect for spherical cavity ($K_t = 2$) compared to a cylindrical cavity ($K_t = 3$).) Accordingly, total strain energy density in the matrix U and its approximated value U' were evaluated for different volume fractions of porosity in the control volume (shown by the broken line). Fig. A-2 shows that, the ratio U'/U is in the range of 0.9–0.92 for the volume fractions studied and hence the assumption is reasonable.

References

1. N. PRIEST and F. VAN DE VYVER, "Trace Metals and Fluoride in Bones and Teeth" (CRC Press, Boca Raton, FL, 1990).
2. R. HAYNES, "The Mechanical Behavior of Sintered Alloys" (Freund Publishing, London, 1981).
3. R. PEKALA, *J. Mater. Sci.* **24** (1989) 3221.
4. K. DENNY, "A Biomechanical Analysis of the Effects of Hand Weights on the Arm-Swing while Walking and Running," Microform, University of Oregon, 1996.
5. R. BOURCIER *et al.*, *Acta Metall.* **34**(12) (1986) 2443.
6. M. ASHBY, *ibid.* **37** (1989) 1273.
7. R. RICE, "Porosity of Ceramics" (Dekker, New York, 1998).
8. L. GIBSON, M. ASHBY, G. SCHAJER and C. ROBERTSON, *Proc. R. Soc.* A **382** (1982) 25.
9. L. GIBSON and M. ASHBY, *Proc. R. Soc. Lond.* A **382** (1982) 43.
10. S. MAITI, M. ASHBY and L. GIBSON, *Scripta Metall.* (1984) 213.
11. G. WANG and V. KRSTIC, *Phil. Mag.* A **78**(5) (1998) 1125.
12. V. KRSTIC and W. ERICKSON, *J. Mater. Sci.* **22** (1987) 2881.
13. W. TONG and G. RAVICHANDRAN, *Composites Sci. and Tech.* **52** (1994) 247.
14. L. NIELSEN, *J. Amer. Ceram. Soc.* **73** (1990) 2684.
15. A. ZIMMERMANN, M. HOFFMAN, B. FLINN, R. BORDIA, T. CHUANG, E. FULLER and J. RÖDEL, *ibid.* **81** (1998) 2449.
16. M. KISER, M. HE and ZOK, *Acta Mater.* **48**(10) (1999).
17. V. PARAMESWARAN and A. SHUKLA, *J. Mater. Sci.* **35**(1) (2000).
18. R. YOUNG and P. BEAUMONT, *ibid.* **12** (1977) 684.
19. Z. HASHIN and S. SHTRIKMAN, *J. Mech. Phys. Solids* **10** (1962) 343.
20. *Idem.*, *ibid.* **11** (1963) 127.
21. Z. HASHIN, *J. Applied Mech.* **58** (1991).
22. G. WENG, *Int. J. Engng. Sci.* **22**(7) (1984) 845.
23. V. KRSTIC, U. ERB and G. PALUMBO, *Scripta Metallurgica et Materialia* **29** (1993) 1501.
24. V. KRSTIC, *Acta Metall.* **33**(3) (1985) 521.
25. R. RICE, *J. Mater. Sci.* **32** (1997) 4731.
26. H. TADA, P. PARIS and G. IRWIN, "The Stress Analysis of Cracks Handbook" (Paris Productions, St. Louis, MO, 1985).
27. C. WU and R. RICE, *Ceram. Eng. Sci. Proc.* **6** (1985) 997.
28. G. HOLLENBURG and G. WALTHER, *J. Amer. Ceram. Soc.* **63** (1980) 610.
29. N. DOWLING, "Mechanical Behavior of Materials" (New Jersey, 1993).
30. N. O'DOWD, C. SHIH and M. STOUT, *Int. J. Solid Structures* **29**(5) (1992) 571.
31. L. XU and H. V. TIPPUR, *Int. J. Fract.* **71** (1995) 345.

Received 20 December 2000
and accepted 22 October 2001